Transport of Passive Tracers in Baroclinic Wave Life Cycles

ELIZABETH M. STONE* AND WILLIAM J. RANDEL

National Center for Atmospheric Research, Boulder, Colorado

JOHN L. STANFORD

Department of Physics and Astronomy, Iowa State University of Science and Technology, Ames, Iowa

(Manuscript received 19 March 1997, in final form 9 June 1998)

ABSTRACT

The transport of passive tracers in idealized baroclinic wave life cycles is studied using output from the National Center for Atmospheric Research Community Climate Model (CCM2). Two life cycles, LCn and LCs, are simulated, starting with baroclinically unstable initial conditions similar to those used by Thorncroft et al. in their study of two life cycle paradigms. The two life cycles LCn and LCs have different initial horizontal wind shear structures that result in distinctive nonlinear development. In terms of potential vorticity–potential temperature (PV–theta) diagnostics, the LCn case is characterized by thinning troughs that are advected anticyclonically and equatorward, while the LCs case has broadening troughs that wrap up cyclonically and poleward.

Four idealized passive tracers are included in the model to be advected by the semi-Lagrangian transport scheme of the CCM2, and their evolutions are investigated throughout the life cycles. Tracer budgets are analyzed in terms of the transformed Eulerian mean constituent transport formalism in pressure coordinates and also in isentropic coordinates. Results for both LCn and LCs show transport that is downgradient with respect to the background structure of the tracer field, but with a characteristic spatial structure that maximizes in the middle to high latitudes. For the idealized tropospheric tracers in this study, this represents a net upward and poleward transport that enhances concentrations at high latitudes. These results vary little with the initial distribution of the constituent field. The time tendency of the tracer is influenced most strongly by the eddy flux term, with the largest transport occurring during the nonlinear growth stage of the life cycle. The authors also study the transport of a lower-stratospheric tracer, to examine stratosphere–troposphere exchange for baroclinic waves.

1. Introduction

Due to their fundamental importance to midlatitude tropospheric dynamics, baroclinic waves have been the focus of several model simulation studies (Simmons and Hoskins 1978, 1980; Gutowski et al. 1989, 1992; Branscome et al. 1989; Barnes and Young 1992; Thorncroft et al. 1993, hereafter THM). These nonlinear and highly idealized simulations have shown that the evolution of the waves can be characterized by a well-defined life cycle of baroclinic growth, maturity, and barotropic decay.

Of particular interest have been the two paradigms of life cycle evolution, LC1 and LC2, described by THM [originally denoted the ''basic'' and ''anomalous'' cases by Simmons and Hoskins (1980)]. They simulated two idealized zonal wave 6 life cycles with initial mean flows that differed only in the strength and sense of the horizontal shear of the zonal wind. This difference in horizontal shear strongly influenced the type of behavior that ensued. In the initial growth stage the waves evolve similarly but become different during their nonlinear mature stages. The two paradigms are characterized in terms of ''cyclonic'' and ''anticyclonic'' behavior, referring to the airflow pattern along isentropic surfaces. LC1 exhibits predominately anticyclonic behavior and is characterized as an equatorward wave-breaking event. In terms of potential vorticity–potential temperature (PV–theta) diagnostics (Hoskins et al. 1985), LC1 portrays northeastward to southwestward tilted thinning troughs that are advected anticyclonically and equatorward. The life cycle consists of baroclinic growth followed by barotropic decay with poleward momentum fluxes. LC2 has northwestward- to southeastward-tilting broadening troughs that wrap up cyclonically and poleward (deemed purely cyclonic behavior) producing cutoff cyclones at high latitudes. Lee and Feldstein (1996) describe a further analysis of the wave-breaking para-

* Current affiliation: Jet Propulsion Laboratory, California Institute of Technology, Pasadena, California.

Corresponding author address: Dr. Elizabeth M. Stone, Jet Propulsion Laboratory, California Institute of Technology, Mail Stop 183-701, 4800 Oak Grove Drive, Pasadena, CA 91109.

digms by studying cyclonic and anticyclonic wave breaking in an aquaplanet GCM simulation with a full wavenumber spectrum.

The usefulness of the idealized baroclinic wave studies is borne out in their similarity to observational data. The extratropical Southern Hemisphere (SH) summer circulation pattern is frequently dominated by medium-scale, eastward-propagating waves (Salby 1982; Hamilton 1983; Randel and Stanford 1985a,b) that often exhibit well-defined life cycles. Furthermore, both the time-averaged spatial structure and the transient statistical signatures of eddy heat, momentum, and potential vorticity fluxes observed in both the Northern Hemisphere (NH) and SH are similar to characteristics in these idealized life cycles (Randel and Held 1991). This suggests that much of the fundamental dynamics of tropospheric eddies and their interactions with the mean flow can be understood based on the life cycle paradigm. The aim of this work is to develop a similar idealized understanding of tropospheric tracer transport.

The distinction between the two life cycle paradigms of THM is useful for understanding real systems that combine the cyclonic and anticyclonic behavior. THM show examples of the two types of behavior in operational meteorological analyses (see their Fig. 14). Hartmann (1995) studied characteristics of zonal flow vacillation in the SH using 13 yr of global analysis. The two extreme phases of the vacillation revealed fundamentally different synoptic evolutions that are similar to the two life cycle paradigms.

Studies of baroclinic waves have also included their impact on atmospheric constituent distributions. Measurements of total column ozone from the Total Ozone Mapping Spectrometer have revealed baroclinic wave disturbances in the SH (Schoeberl and Krueger 1983) and along NH oceanic storm-track regions (Mote et al. 1991). Stone et al. (1996) investigated medium-scale waves in upper-tropospheric water vapor from the *Upper Atmosphere Research Satellite* (*UARS*) Microwave Limb Sounder.

Our goal in this study is to investigate the behavior of passive tracers during the two types of life cycles. We run a simulation with the National Center for Atmospheric Research (NCAR) Community Climate Model (CCM2), with initial conditions similar to those used in the LC1 and LC2 experiments. The dynamic evolutions of these life cycles are described briefly. We then examine the tracer budgets utilizing the transformed Eulerian mean (TEM) constituent transport formalism in pressure coordinates, with the aim of separating eddy and mean meridional circulation components, and detail the net transport during the wave growth, maturity, and decay stages. We also compare the TEM results with isentropic coordinate transport calculations. Three different tropospheric constituent distributions are advected by the transport scheme of the CCM2 to assess the influence of the initial distribution on the transport characteristics. We furthermore study stratosphere–troposphere exchange in the life cycles by using a tracer with an initial distribution only in the lower stratosphere.

2. Model description and initial conditions

a. Model description

The CCM2 (Hack et al. 1993; Hack et al. 1994) is a three-dimensional atmospheric general circulation model developed at NCAR for the purpose of climate simulation studies and medium- to long-range forecast studies. The simulation analyzed here uses the standard resolution of the CCM2, with triangular wavenumber T42 spectral resolution and 18 vertical levels (992.5, 970.4, 929.3, 866.4, 786.5, 695.2, 598.2, 501.3, 409.0, 324.8, 251.2, 189.2, 138.7, 99.0, 63.9, 32.6, 13.1, 4.8 mb). The T42 resolution corresponds to 128 longitudes and 64 latitudes on a Gaussian spectral transform grid. The vertical coordinate of the model is a hybrid-sigma coordinate that follows the terrain near the surface and becomes purely a pressure coordinate above 100 mb. The model time step is 20 min. The dry dynamical equations are solved by a spectral transform method in the horizontal and finite differences in the vertical. Horizontal diffusion at all model levels except the top three is applied to vorticity, divergence, and temperatures, using a ∇^4 diffusion operator with a coefficient of 10^6 m^4 s^{-1}. Diffusion at the upper model levels is applied with a ∇^2 operator (Hack et al. 1994).

Constituent transport is accomplished by means of a shape-preserving, semi-Lagrangian method (Williamson and Rasch 1989; Rasch and Williamson 1990) applied on the latitude–longitude grid. Horizontal diffusion is not applied to constituents transported by the model. CCM2's constituent transport abilities have been utilized in studies of water vapor transport (Williamson and Rasch 1994), the seasonal cycle of CO_2 (Erickson et al. 1996), and the transport of $CFCl_3$ (Hartley et al. 1994). Zapotocny et al. (1996) and Zapotocny et al. (1997) examine the transport and conservation abilities for inert trace constituents in the CCM2.

Several alterations to the standard configuration of the CCM2 were made for the simulations in this study. An adiabatic version of the model was used, which eliminated radiative heating and moist physical processes (convection, precipitation, evaporation, and temperature adjustment due to latent heating). At each time step of the simulation, model fields were truncated to retain only their zonal mean, zonal wave 6, and wave 6 harmonic values. An aquaplanet was simulated by setting the surface type and boundary conditions to oceanic values everywhere on the model surface.

b. Initial conditions

Since the model simulations are done with adiabatic, aquaplanet conditions, there is no difference between the two hemispheres simulated by the model. Given this,

and the fact that the timescales of the integrations are short enough such that there is little interhemispheric interaction, one model run can be used to simulate two life cycles simultaneously, one in each hemisphere. The initial zonal wind fields for the NH and SH of the model simulation, shown in the top panel of Fig. 1, were designed to be similar to the wind fields of the LC1 and LC2 cases of THM, respectively. The wind field in the SH is identical to that of the NH, but with an added barotropic component that is -10 m s^{-1} at 50°C and 10 m s^{-1} at 20°S. The jet core in each hemisphere is near the 200-mb level with maximum velocities of 43 m s^{-1} in the NH and 35 m s^{-1} in the SH. The NH of the model will be used to simulate the LCn (''n'' for no additional horizontal shear and north) case and the SH for the LCs (''s'' for increased horizontal shear and south) case. Subsequent plots show both cases simultaneously, LCn in the NH and LCs in the SH.

The initial perturbations in the zonal and meridional wind, temperature, and surface pressure fields were obtained from a model calculation using a linear version of CCM2 (G. Branstator 1994, personal communication). The fastest growing zonal wave 6 structure from this model output was normalized to a 1-mb surface pressure perturbation and added to the initial zonal mean fields.

The simulation included four passive tracers (χ_1–χ_4) to be advected by the transport scheme of the CCM2. The numerical values representing the mixing ratios of these passive tracers are arbitrary. The midlatitude tracer χ_1 has a maximum in each hemisphere at 45° and decreases in value symmetrically toward the poles and equator with decreasing pressure. Although idealized, χ_1's structure represents a tracer with a low-level, midlatitude source (such as fossil fuel CO_2). The tracer χ_2 is a vertically stratified tracer with an initial vertical gradient of 10 km^{-1}, and χ_3 is a horizontally stratified tracer with its largest values occurring at the equator and a meridional gradient of 2 (deg lat)$^{-1}$. The tracers χ_2 and χ_3 were constructed to be orthogonal to each other such that we could assess the influence of the meridional and vertical tracer gradients on the transport characteristics associated with the baroclinic wave event. The tracer χ_4 is a step function tracer, initialized with a value of unity in the stratosphere (above the tropopause) and zero in the troposphere. The tropopause was defined here by the PV = 2 PVU (1 PVU = 10^{-6} m^2 K s^{-1} kg^{-1}) location in the middle and high latitudes and the 380-K potential temperature surface in the Tropics. Poleward of 60°, the 2 PVU-surface is at approximately 8 km. The 2 PVU- and 380-K surfaces intersect near 15° and 14 km. The stratospheric tracer is used to analyze the effect of the baroclinic waves on transport near the tropopause.

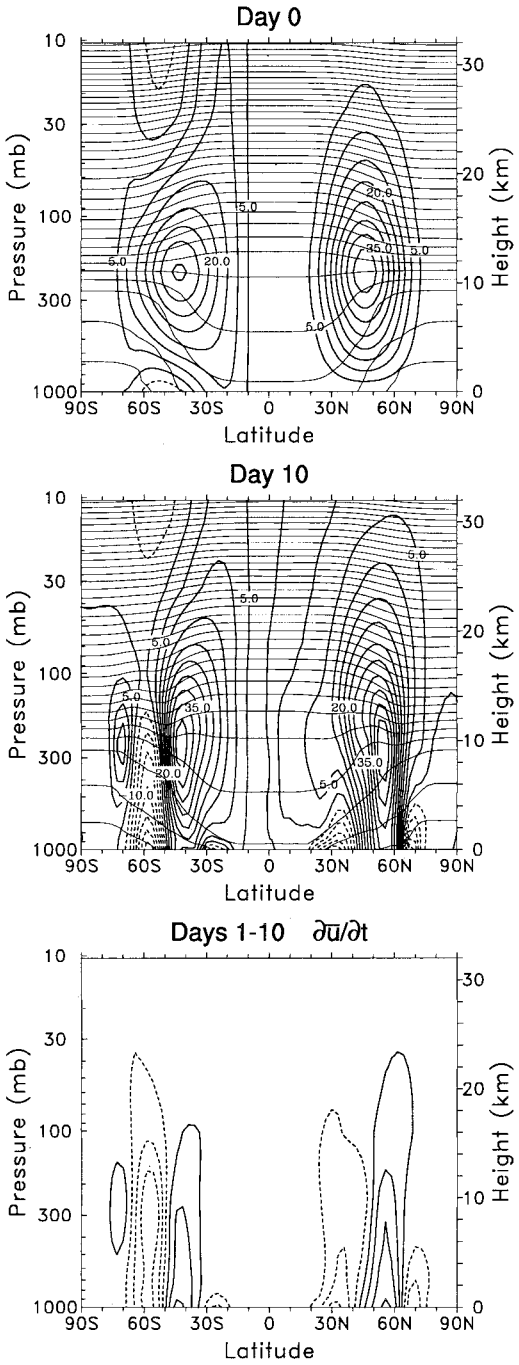

FIG. 1. Zonal mean zonal wind (contour interval of 5 m s^{-1}) and potential temperature field (contours of 260, 280, 300, . . . K) on (top) day 0 and (middle) day 10; (bottom) the time tendency of the zonal wind averaged over days 1–10 of the simulation with contours of ±0.5, 1.5, 2.5, . . . m s^{-1} day^{-1}.

3. Life cycle description

The model simulation analyzed for this study is an 18-day run initialized as described in the previous section and run in an adiabatic version of the CCM2. Two life cycles, LCn and LCs, are produced as output. The evolution of the channel-integrated (866–13 mb, 30°–60°) eddy kinetic energy is shown in Fig. 2. The two cases show similar energy evolution over the first 10

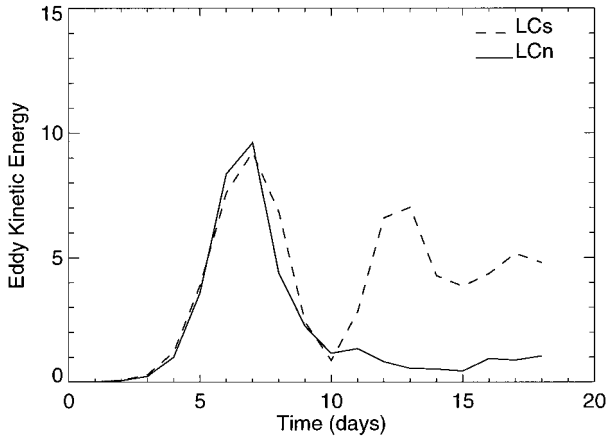

FIG. 2. The time evolution of eddy kinetic energy. The solid (dashed) line represents LCn (LCs) energy values. Ordinate values represent energy per unit area in 10^5 J m^{-2}.

days of the run with regard to amplitude and growth and decay rates. The maximum eddy kinetic energy occurs on day 7. After day 10 of the simulation, the eddy kinetic energy of the LCn case remains small while LCs has a second growth and decay cycle. The discussion that follows will focus on the first growth and decay cycle (days 0–10) of the two cases. Despite the similarity in the eddy kinetic energy for the two cases over this 10-day time period, seen in Fig. 2, the following results show significant differences in their life cycle evolutions.

A comparison of the initial wind field with that of day 10 (Fig. 1) shows that the jet of LCn (displayed in the NH) moves about 10° poleward during the life cycle while the jet core of the LCs (displayed in the SH) moves a few degrees equatorward during this time. Both jets are more barotropic on day 10. The time-averaged tendency of the zonal wind, $\partial\overline{u}/\partial t$, is also shown in Fig. 1. The two life cycles display nearly opposite tendency patterns. The zonal wind tendency of LCn is positive poleward of the initial jet core location and negative equatorward of it. The positive and negative regions are reversed for the LCs case.

Eliassen–Palm (EP) flux diagrams (Edmon et al. 1980) are useful to depict the direction and relative importance of eddy heat and momentum fluxes along with the net wave forcing of the zonal mean flow. The EP flux vectors also denote the direction of wave group velocity in the meridional plane (in the WKB limit). Figure 3 displays EP flux diagrams for three time segments in the life cycles (growth, maturity, and decay). During the initial days of baroclinic growth, both LCn and LCs show convergence and vertical EP flux vectors (poleward heat flux) confined to low levels of the midlatitudes. The convergence region moves into the upper troposphere during days 5–7, corresponding to the vertical propagation of wave activity. At this time, a difference between the two cases becomes apparent. The

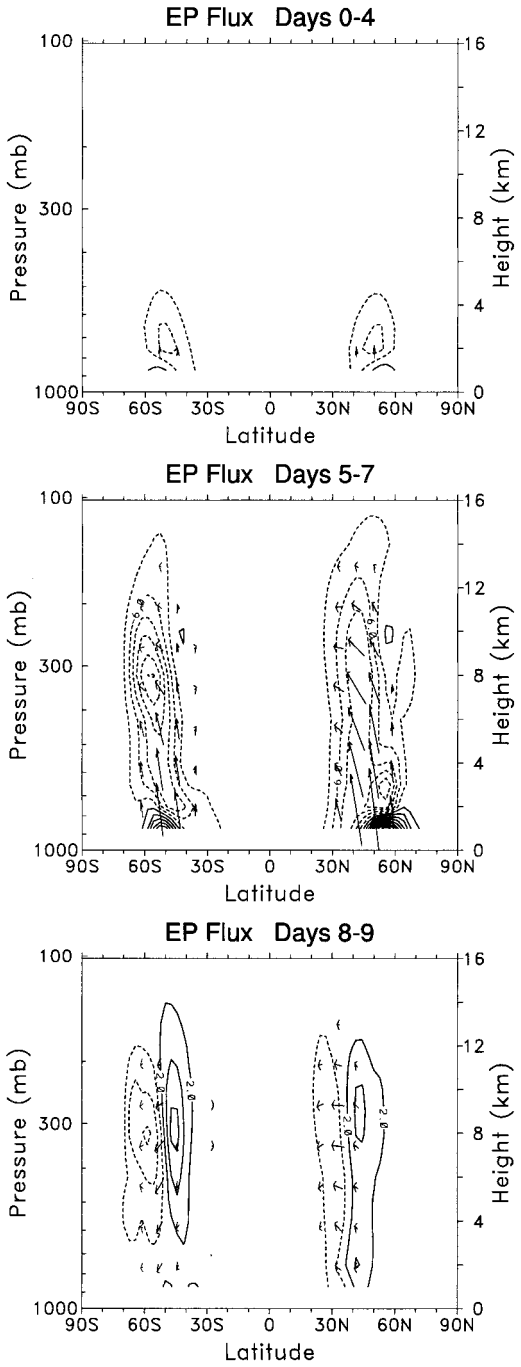

FIG. 3. The EP flux vectors and divergence (contours of ±3, 9, 15, . . . m s^{-1} day^{-1}) averaged over days (top) 3–4, (middle) 5–7, and (bottom) 8–9 of the life cycle.

LCn vectors turn equatorward in the upper troposphere identifying equatorward wave propagation (poleward momentum flux). In the LCs case, the EP flux vectors turn poleward (equatorward momentum flux) and are not as strong as their LCn counterparts. The LCs structure suggests that the wave activity is more confined to high latitudes than for LCn.

The EP flux diagrams for days 8–9 also show a marked difference between the two life cycles. Each has a divergence–convergence pair centered in the upper troposphere but with opposite polarity. In the case of LCn, the convergence region is equatorward of 40°N and the divergence is poleward of this latitude. The vectors are predominantly horizontal and point equatorward. LCs has a reversed pattern of divergence and convergence, as compared with LCn, and is centered at higher latitudes. In this case, the vectors point poleward and slightly downward. As previously noted, the EP flux divergence represents the net influence of the eddies on the zonal mean flow. Note that the convergence–divergence pairs shown in the bottom panel of Fig. 3 are similar to the alternating patterns of positive and negative tendency of the zonal wind field over the course of the life cycle (Fig. 1).

The two life cycles can also be compared and contrasted in terms of their synoptic evolution. Four-day sequences of potential vorticity distributions on the 315-K surface are shown in Figs. 4 and 5 for the LCn and LCs cases, respectively. The 315-K surface is at ~10 km in the polar regions and ~4 km in the Tropics. The PV fields in the two hemispheres look similar on day 5. However, a marked difference is apparent in their subsequent development. For LCn, the trough axis tilts in the northwest to southeast direction poleward of 50°N and in the northeast to southwest direction equatorward of this. On days 6 and 7, the contours of PV wrap up cyclonically poleward of 55°N while equatorward of this they are drawn out to the south and west. In this way, the life cycle exhibits both cyclonic and anticyclonic behavior. The wave trough thins and is stretched farther in the southwestward direction such that by day 8 cutoff regions form. The wave is more zonal in the higher latitudes at this time. In contrast to this development, the LCs wave is tilted predominantly in the southwest to northeast direction in the SH. On day 6 the contours of PV begin to wrap up cyclonically. This wrapping up occurs on a larger scale than that in the LCn case. Isolated vortices of near-constant PV values are present on days 7 and 8. These vortices have a broad zonal structure and do not reach the low latitudes as in LCn, consistent with the EP flux diagrams in Fig. 3. This case consists predominately of cyclonic behavior. By day 10 (not shown) the vortices have dissipated.

The life cycle diagnostics described above for LCn and LCs are similar, but not identical, to the results reported for LC1 and LC2 by THM (with LCn and LCs corresponding to the LC1 and LC2 experiments, respectively). The main difference between the simulations is the rate of decay of the LCs case here compared with LC2 in THM. After reaching its peak value, the kinetic energy in LC2 levels off without decaying completely and does not have a second growth and decay cycle as is seen in LCs. Correspondingly, the vortices that form in the cyclonic wrapping up of PV contours are much more persistent in LC2 than those in our LCs

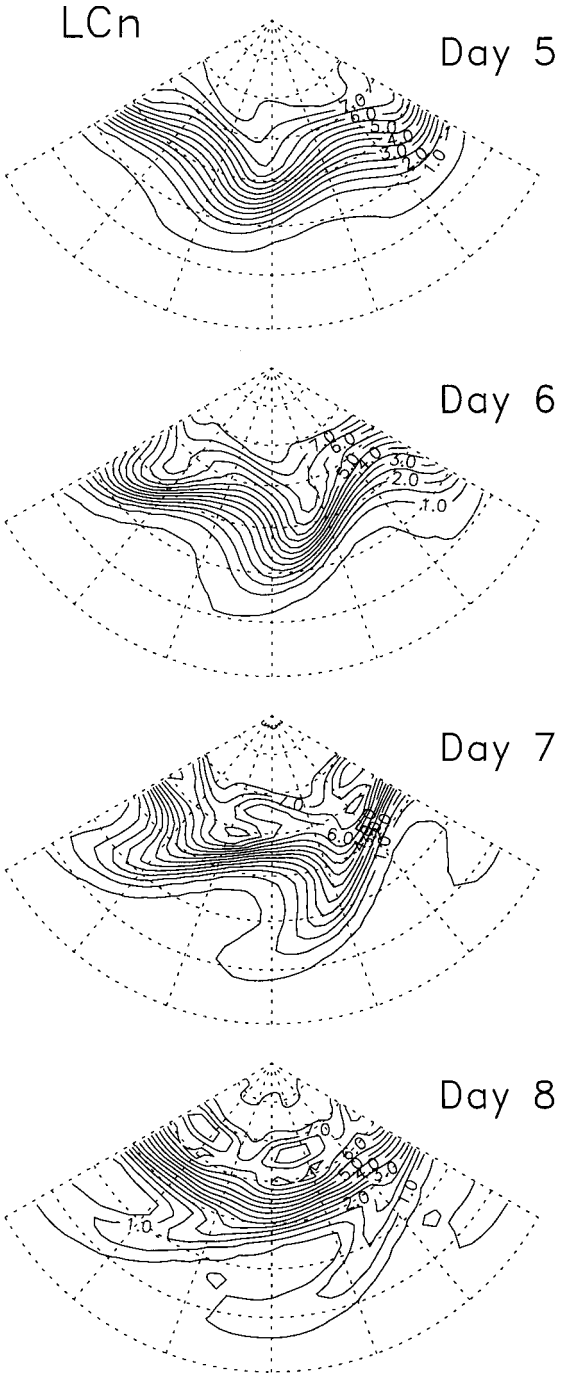

FIG. 4. Potential vorticity on the 315-K potential temperature surface for days 5–8 of LCn displayed in the NH. Contours are 0.5, 1.0, 1.5, . . . 10^{-6} m^2 s^{-1} K kg^{-2}. The sectors shown represent two zonal wavelengths with meridional coverage from 20°N to the pole. Lines of constant latitude and longitude are drawn every 10° and 20°, respectively.

results. LC2 also reaches a higher maximum value of eddy kinetic energy than LC1, while we find similar maximum values for LCn and LCs. Magnusdottir and Haynes (1996) studied wave diagnostics of four differ-

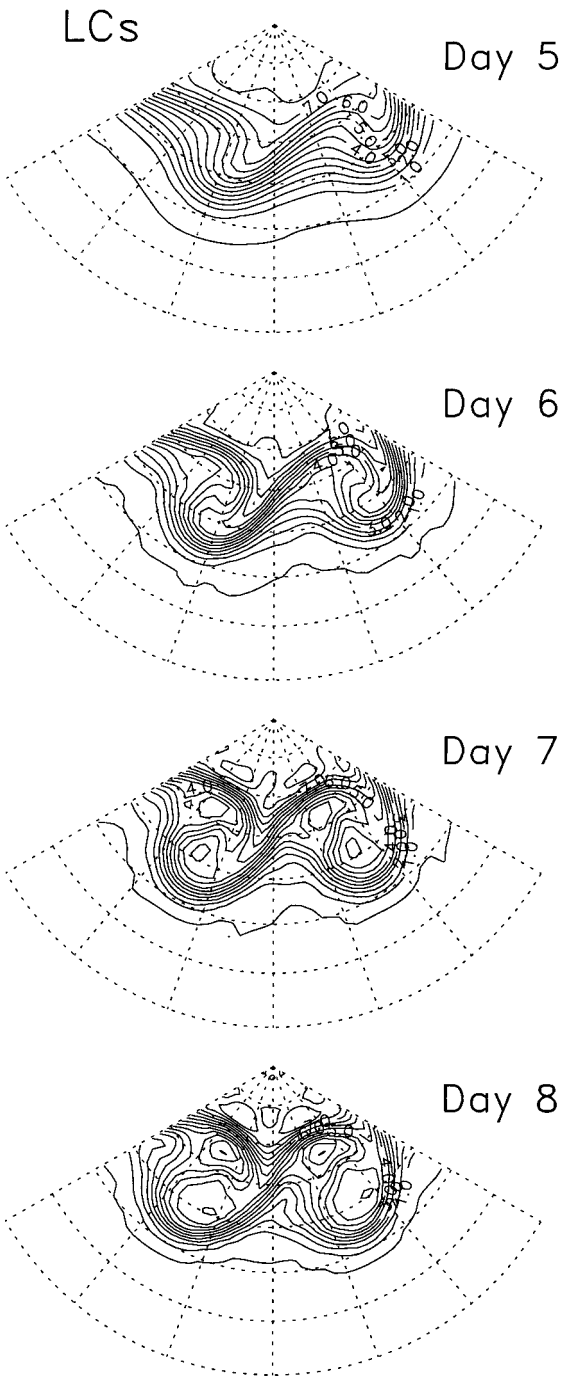

FIG. 5. Potential vorticity on the 315-K potential temperature surface for days 5–8 of LCs displayed in the SH. Contours (0.5, 1.0, 1.5, . . . 10^{-6} m^2 s^{-1} K kg^{-2}) are in absolute values. The sectors shown represent two zonal wavelengths with meridional coverage from 20°S to the pole. Lines of constant latitude and longitude are drawn every 10° and 20°, respectively.

ent baroclinic wave life cycles, including LC1 and LC2 of THM. Their findings show the classification of the two paradigms to be robust in terms of the PV field and wave activity diagnostics. The cases were not found to be distinct in terms of the eddy kinetic energy, suggesting that this diagnostic may not sufficiently distinguish between the two paradigms. As shown in Figs. 3–5, despite the nearly identical kinetic energy evolutions, the LCn and LCs cases represent fundamentally different dynamical behavior. A second difference between our results and those for LC1 and LC2 is seen in the strength of the momentum fluxes of LCs and LC2. The simulation in this study produced a much stronger equatorward flux in the later stages of LCs than that reported for LC2, and this is linked with the stronger decay of this case, as measured by the eddy kinetic energy of LCs.

The overall appearance of cyclonic and anticyclonic behavior for the two different initial conditions is similar for both simulations and the minor differences are not the focus of this study. Possible sources of discrepancy between this simulation and that of THM are the model resolution and the strength of the horizontal diffusion. The model diffusion, in particular, may affect the timescale on which the wave decays.

4. Tracer transport

a. Zonal mean description

The transport that occurs during the life cycles can be observed in changes in the tracer fields and in regions of positive and negative tracer tendency. Figure 6 shows meridional cross sections of the horizontally stratified tracer, the vertically stratified tracer, and the midlatitude tracer at the start and end of the life cycle. The difference in the tracer field over this time period is shown as the time-averaged tendency (Fig. 6b). Sharper meridional gradients are formed for all three tracers during the life cycles near the 60°–70° latitude range of LCn and LCs above 600 mb. Positive tendency values are seen in this region that peak at 300–400-mb altitude, corresponding to an increase in tracer value over the life cycle. LCn has a broader region of positive tendency, with two peaks about 10° apart, than that seen in LCs. The region extends from 40°–70°N, with the exception being the midlatitude tracer, which has a somewhat narrower structure. The region of positive tendency in LCs is confined to the 55°–75°S range. Negative tendencies exist at the lower levels in the 30°–60° latitudinal range and extend upward from the surface in narrow bands centered near 30°N and 45°–50°S. The net effect displayed in Fig. 6 is that of upward and poleward transport in the troposphere for latitudes ~30°–75° for both the LCn and LCs life cycles. This transport is downgradient with respect to the background tracer distributions. The strongest tracer transport effects are seen near the high-latitude tropopause, poleward of the peak regions of

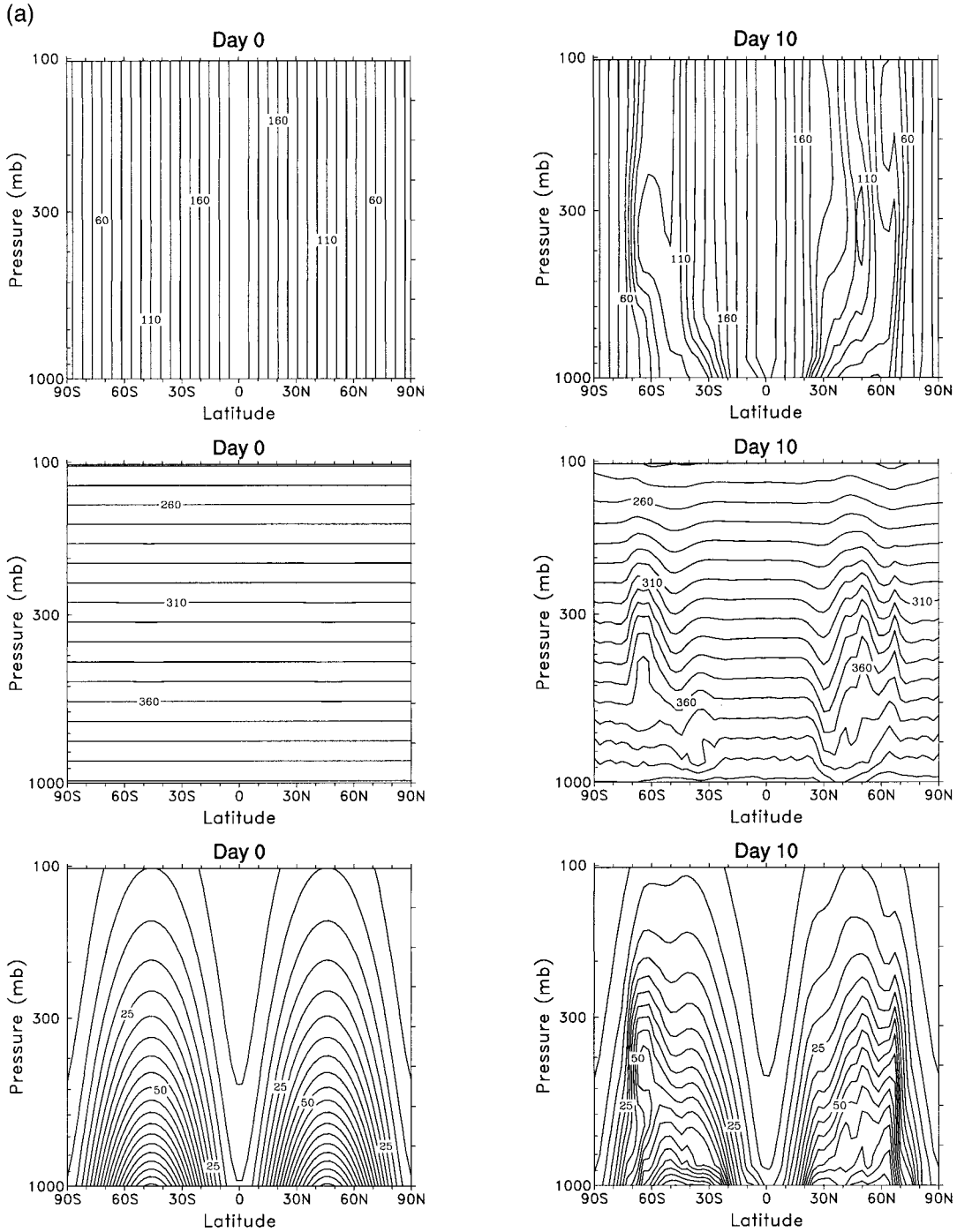

FIG. 6a. The zonal mean tracer fields on day 0 and day 10 for the horizontally stratified tracer (contour interval of 10 kg kg^{-1}), the vertically stratified tracer (contour interval of 10 kg kg^{-1}), and the midlatitude tracer (contour interval of 5 kg kg^{-1}) in the top, middle, and bottom rows, respectively.

eddy activity. The three tracers show very similar tendency structures despite the substantial differences in their initial configurations. Because of this similarity, we focus on the details of transport for the horizontally stratified tracer only.

Figure 7 shows a latitude versus time plot of the horizontally stratified tracer on the 315-K surface, highlighting the change in the meridional gradient of the tracer. The gradient in LCs is increased poleward of 60° but is weakened in the midlatitudes. The meridional tracer gradients of LCn on this surface were increased in two bands centered at 55°N and 75°N. The largest

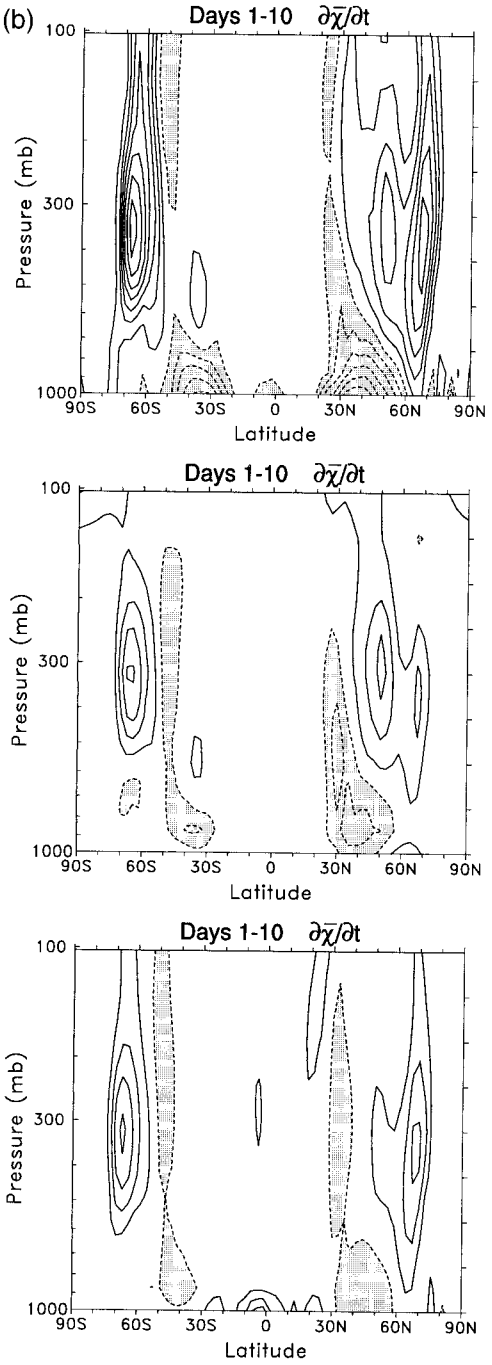

FIG. 6b. The time tendency of the zonal mean tracer fields averaged over days 1–10 of the model run for the three different tracers. Tendency contours are in ±1%, 3%, . . . for the horizontally stratified tracer and the midlatitude tracer and ±0.1%, 0.3%, . . . for the vertically stratified tracer. Shaded regions indicate negative contours.

changes occur between days 5 and 8. In both cases, the field changes relatively little after day 10. The second pulse of eddy activity in the LCs case (see Fig. 2) has the effect of decreasing the meridional tracer gradients near 30°N.

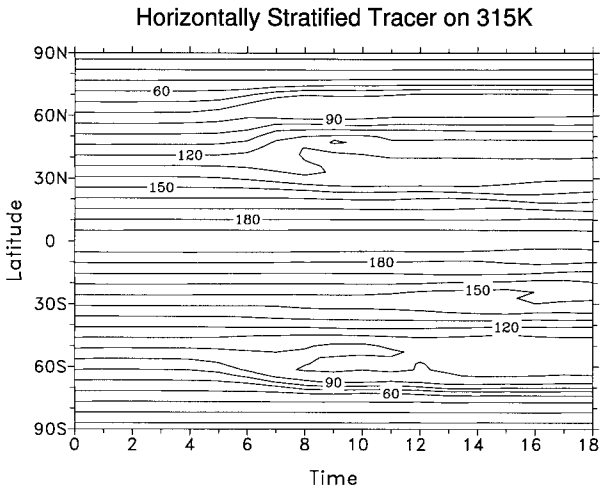

FIG. 7. Latitude vs time plot of the zonal mean of the horizontally stratified tracer on the 315-K potential temperature surface. Contours are in increments of 10 kg kg^{-1}.

b. Tracer budget analysis

In order to study the transport of the zonal mean mixing ratio in the meridional plane associated with the developing baroclinic waves, we make use of the tracer conservation equation based on the TEM formalism in log pressure (z) coordinates [Andrews et al. 1987, Eq. (9.4.13)]:

$$\frac{\partial\overline{\chi}}{\partial t} = -\overline{v}^*\frac{\partial\overline{\chi}}{\partial y} - \overline{w}^*\frac{\partial\overline{\chi}}{\partial z} + \rho_0^{-1}\nabla\cdot\mathbf{M} + \overline{S}. \quad (1)$$

Here $\overline{v}^*$ and $\overline{w}^*$ are components of the residual mean circulation, $\rho_0^{-1}\nabla\cdot\mathbf{M}$ is the eddy transport term, and $\overline{S}$ is a source or sink term, equal to zero for the passive tracers used here. The TEM eddy flux vector $\mathbf{M}$ has components

$$M^{(y)} = -\rho_0\left(\overline{v'\chi'} - \frac{R}{H}\frac{\overline{v'T'}}{N^2}\overline{\chi}_z\right) \quad (2a)$$

$$M^{(z)} = -\rho_0\left(\overline{w'\chi'} + \frac{R}{H}\frac{\overline{v'T'}}{N^2}\overline{\chi}_y\right). \quad (2b)$$

Note that these terms are related to the negative of the Eulerian mean tracer fluxes. Here $M^{(y)}$ and $M^{(z)}$ are also dependent on the product of the eddy heat flux and the vertical or meridional tracer gradient.

Equation (1) defines the zonal mean tracer tendency in terms of transport due to advection by the residual circulation ($\overline{v}^*$ and $\overline{w}^*$ terms), transport due to eddy tracer flux divergence ($\rho_0^{-1}\nabla\cdot\mathbf{M}$), and sources and sinks. The nontransport theorem (Andrews et al. 1987) states that for linear, steady, adiabatic, conservative waves, the residual circulation and the eddy flux divergence are identical to zero, and under these conditions, no net meridional transport occurs. However, the conditions of nontransport are violated by the lack of

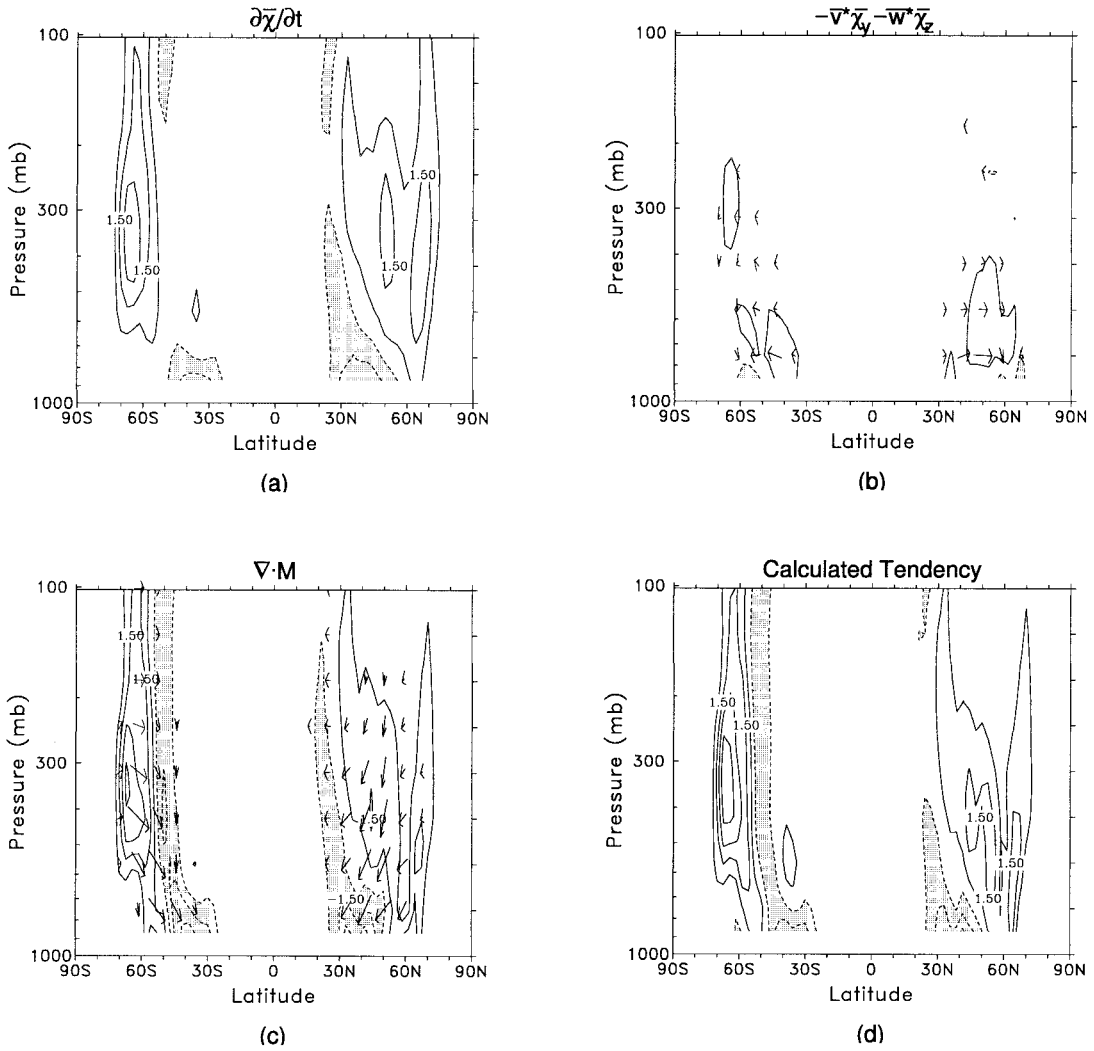

FIG. 8. Individual terms in the tracer continuity equation [Eq. (1)] for the horizontally stratified tracer averaged over days 1–10 of the model simulation. (a) Tracer tendency; (b) residual mean circulation tendency with arrows indicating the circulation ($\overline{v}^*$, $\overline{w}^*$); (c) eddy flux divergence tendency with arrows indicating the components of the vector **M**; (d) sum of the mean circulation tendency and the eddy flux divergence tendency. Contours are of ± 0.5, 1.5, 2.0, . . . g kg^{-1} day^{-1}. Shaded regions indicate negative contours.

steadiness and the nonlinear dynamics of baroclinic waves, and we detail here the balances in Eq. (1) throughout the life cycles.

The four panels in Fig. 8 depict the tracer tendency, the advection by the residual mean circulation, the wave transport effects, and the calculated tendency, which is the sum of the latter two. The calculations are averaged over days 1–10 of the model run for the horizontally stratified tracer. A comparison of the measured and calculated tendencies (Figs. 8a and 8d) shows that the equation balances relatively well. The structure of the calculated and actual tendency is similar, although in magnitude, they are not a perfect match. Reasons for this difference may be the interpolation from the model levels to pressure surfaces and the finite difference approximations used for calculations of derivatives in the equation.

Figure 8 also shows that over the 10 days of the life cycles, the balance of the equation is approximately between the tendency and the eddy tracer flux divergence, $\partial\overline{\chi}/\partial t \approx \rho_0^{-1}\nabla \cdot \mathbf{M}$. The advection by the residual mean flow plays only a small role. The tendency and eddy flux divergence attain their maximum values at the 300–400-mb level in the extratropics. There is convergence and negative tendencies at the lower levels equatorward of this. Overall, the eddy fluxes act to increase the constituent values in the upper troposphere at latitudes poleward of 50°.

Figure 9 displays the two dominant terms in Eq. (1), and the tracer tendency and the eddy flux divergence.

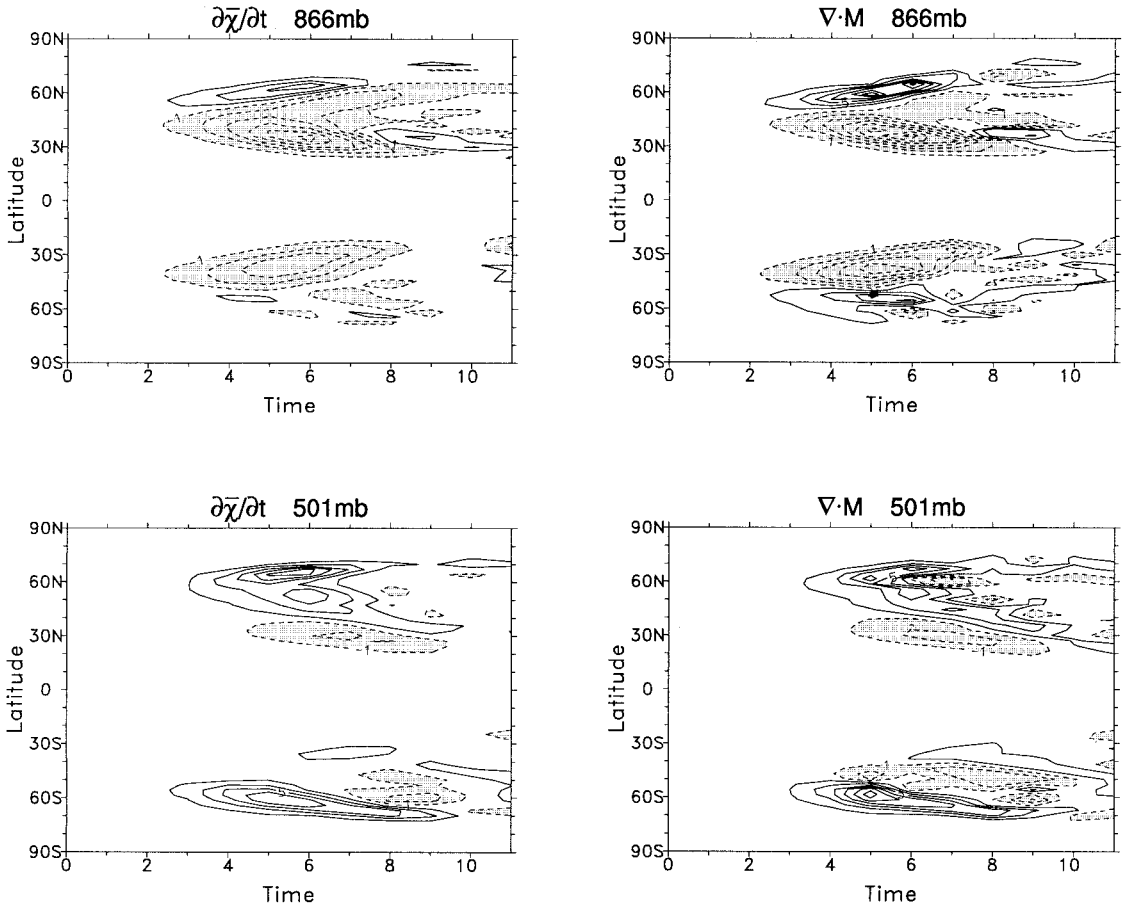

FIG. 9. Latitude–time sections of the horizontally stratified tracer tendency and the eddy flux divergence tendency on the 866- and 501-mb pressure surfaces for days 0–11 of the life cycle.

The time evolution of the two quantities are displayed on latitude versus time grids at the 866- and 501-mb levels, showing the development of the eddy tracer transport and total tracer transport throughout the life cycles. Approximate balance between these two terms is seen with the eddy flux divergence being slightly larger in magnitude than the tendency term. On the lower surface, the region of negative tendency (and corresponding eddy flux convergence) in each life cycle moves equatorward with time from 45° to 25°, peaking on days 5–6. LCn has a broader meridional structure with negative tendencies extending poleward with time as well. In the middle troposphere, the region of positive tendency (or flux divergence) moves poleward with time from 55° to 70° in both cases. LCn again has a broader structure. The negative tendency region is equatorward and weaker than the positive region.

Also included in the diagram of eddy flux divergence (Fig. 8c) are vectors depicting the components of the TEM eddy flux vector, $M^{(y)}$ and $M^{(z)}$. These cross sections showing the direction and magnitude of the TEM eddy tracer flux and its divergence are analogous to EP flux cross sections (Edmon et al. 1980). In plotting the vectors, the density factor in Eq. (2) is omitted, and $M^{(z)}$ is multiplied by a factor of 150 (the approximate ratio of N/f) so that $M^{(y)}$ and $M^{(z)}$ are plotted isotropically in the latitude–height plane [in analogy with EP flux diagrams; see Palmer (1982)]. Note that, by definition [Eqs. (1) and (2)], the vectors are in the opposite direction to the eddy tracer fluxes so that divergence of **M** corresponds to positive tracer tendency. The overall features of the eddy tracer flux and its divergence are similar for the two life cycles, showing **M** vectors that point downward and equatorward (signifying eddy tracer fluxes that are upward and poleward). Both the horizontal and vertical flux components contribute significantly to the eddy transport. However, the detailed transport characteristics are somewhat different between LCn and LCs. The wave transport for LCn displays a broader meridional region of convergence in the middle to high latitudes, and the wave flux patterns extend much more into the subtropics than those for LCs (which appear confined to high latitudes). This asymmetry is qualitatively similar to differences in the EP flux diagrams discussed above.

In analogy to Fig. 3, Fig. 10 breaks down the eddy

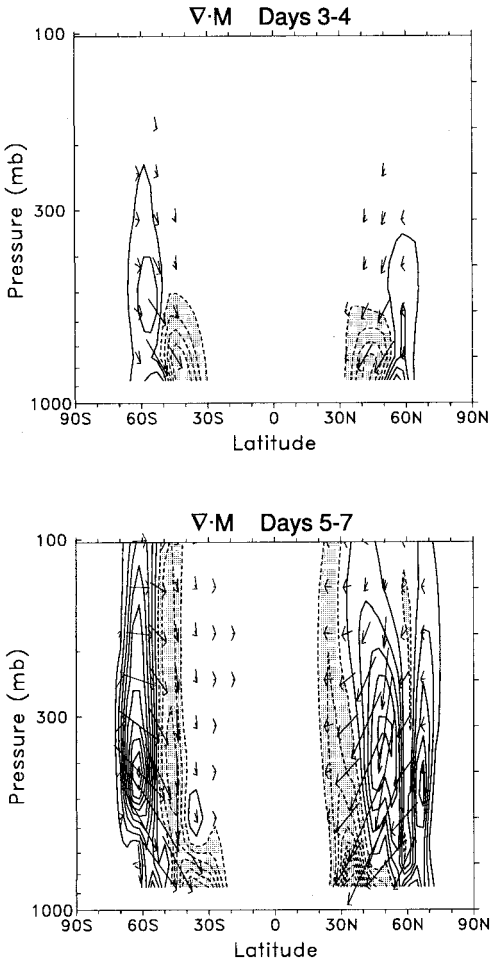

FIG. 10. Meridional cross sections of the eddy flux divergence tendency for the horizontally stratified tracer with arrows indicating the components of the vector **M** for days (upper) 3–4 and (lower) 5–7. Contours a reshown in increments of 1 g kg^{-1} day^{-1} and negative regions are shaded.

flux divergence and vectors into two time segments to demonstrate the stages of development of the wave transport effects. The wave transport term was shown to be the dominant influence on the changes to the tracer field. Regions of divergence (positive contours) indicate increasing tracer values. Early on in the life cycles, the divergent and convergent regions peak at the lower levels of the midlatitudes with the convergence of eddy tracer flux occurring equatorward of the divergent regions. During the mature phase of the waves (days 5–7), strong eddy transports are found in the middle and upper troposphere, and more asymmetry is found between LCn and LCs. Peak values of the divergence remain at the lower levels, while the positive regions peak around 400 mb. During this time, the strongest changes in the zonal mean tracer field occur. The vectors of eddy flux point predominately downward and equatorward in both cases, indicating that eddy transports are upward and poleward.

This section has focused primarily on analysis of the horizontally stratified tracer since, as noted in Fig. 6, the three different tracer tendencies were similar over the life cycles. Figure 11 displays the wave transport term of Eq. 1 for the vertically stratified tracer and the midlatitude tracer averaged over days 3–4 and 5–7. This should be compared with Fig. 10, which shows similar plots for the horizontally stratified tracer. The eddy flux divergence pattern is similar for the three tracers during the growth and mature stages of the life cycles, although the vertical extent of their features and the relative magnitudes of divergent and convergent regions varies among them. Some difference in the wave transport for the three passive tracers is found in the eddy flux vectors. As noted in Fig. 8c, both the horizontal and vertical flux components contribute to the eddy flux vectors. In addition, the two terms that make up $M^{(y)}$ and $M^{(z)}$ [see Eq. (2)] each contribute to the magnitude of the vector components. While in general the structure of the $M^{(y)}$ and $M^{(z)}$ fields is similar for the three tracers discussed here, the relative importance of the two components and the contributions of the terms that form them is sensitive to the distinct gradients of the tracers.

c. *Isentropic calculations*

The use of potential temperature as a vertical coordinate (isentropic coordinates) has the advantage that the ''vertical velocity'' ($D\theta/Dt$) simply equals the diabatic heating rate. Thus, for the adiabatic life cycles analyzed here, tracer transport is expected to occur primarily by eddy transfer along isentropic surfaces. Comparison of the time-averaged eddy transport vectors (**M**) for the horizontally stratified tracer with the time mean isentropes (shown in Fig. 12) confirms this expectation qualitatively: the **M** vectors are approximately parallel to the isentropes for both life cycles, suggesting the transport is primarily isentropic.

The isentropic transport is explored in further detail by analysis of the Eulerian zonal mean transport equation in isentropic coordinates [Andrews et al. 1987, Eq. (9.4.21)]:

$$\frac{\partial \overline{\chi}}{\partial t} = -\overline{v}^{\sigma}\frac{\partial \overline{\chi}}{\partial y} - \overline{\sigma}^{-1}\frac{\partial}{\partial t}(\overline{\sigma'\chi'}) - \overline{\sigma}^{-1}\frac{\partial}{\partial y}(\overline{\sigma v'\chi'}). \quad (3)$$

Here, $\sigma = g^{-1}\partial P/\partial\theta$ is the density in isentropic coordinates, $\overline{v}^{\sigma} = (\overline{\sigma v})/\overline{\sigma}$ is the mass-weighted mean meridional velocity, and diabatic heating and tracer source terms have been omitted.

Figure 13 shows separate terms in the isentropic transport balance [Eq. (3)] for the horizontally stratified tracer life cycle. Individual model fields were interpolated to isentropic levels, followed by explicit calculation of Eq. (3). The term $-\overline{\sigma}^{-1}\partial(\overline{\sigma'\chi'})/\partial t$ is very small and is not included in Fig. 13. The results in Fig. 13 show reasonable agreement between the calculated and observed tendencies, confirming an approximate balance in Eq. (3). The isentropic eddy flux term dominates the

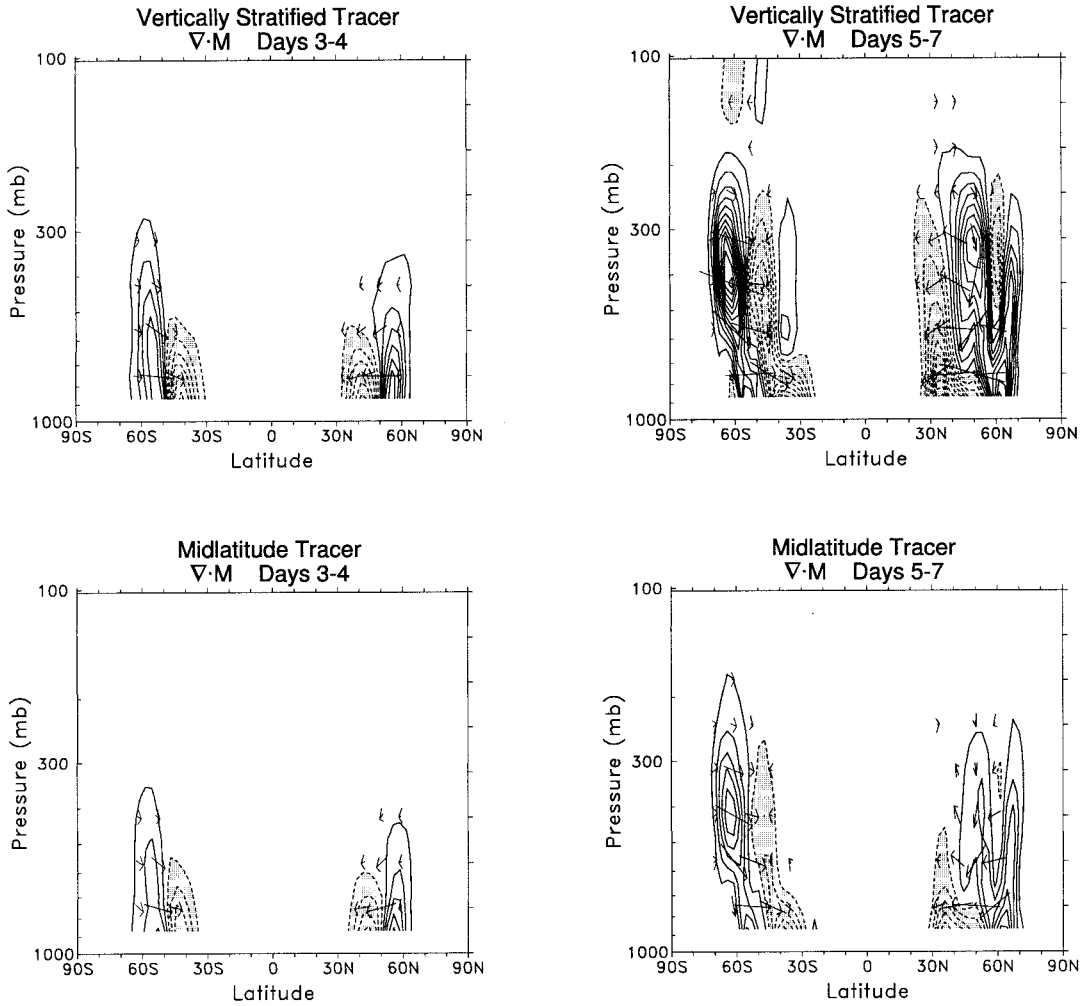

FIG. 11. Meridional cross section of $\nabla \cdot \mathbf{M}$ for the vertically stratified tracer (top) and the midlatitude tracer (bottom) averaged over days 3–4 and 5–7 of the life cycle.

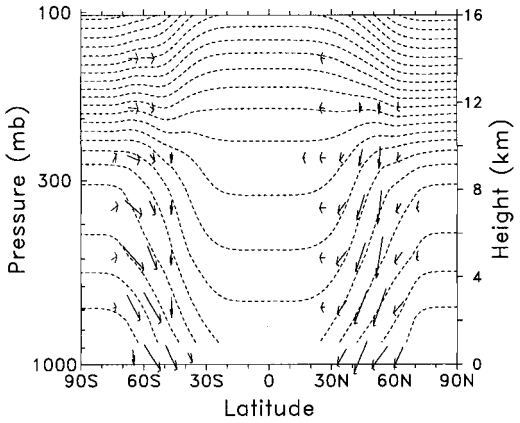

FIG. 12. The time mean isentropes (dashed lines) and the time-averaged eddy transport vectors **M**. Contours are of 260, 280, 300, . . . K.

transport in Fig. 13, with relatively small contribution from the mean meridional transport term (although there is no mean cross-isentropic velocity in this calculation, there is a nonzero $\overline{v}^{\sigma}$ due to the redistribution of mass during the life cycle). We note that the tracer transport viewed in the Eulerian mean isentropic framework [Eq. (3) and Fig. 13] closely resembles the results in the transformed Eulerian mean log pressure coordinates [Eq. (1) and Fig. 8]. These results also confirm that the baroclinic wave tracer transport studied here is predominantly isentropic in nature.

d. Synoptic description

The overall behavior of tracer transport is similar for LCn and LCs when viewed in a zonally averaged perspective (e.g., Fig. 8), although the extension of LCn to the subtropics and confinement of LCs to higher latitudes is apparent. Synoptic pictures of the tracers during the life cycles serve to emphasize the different features

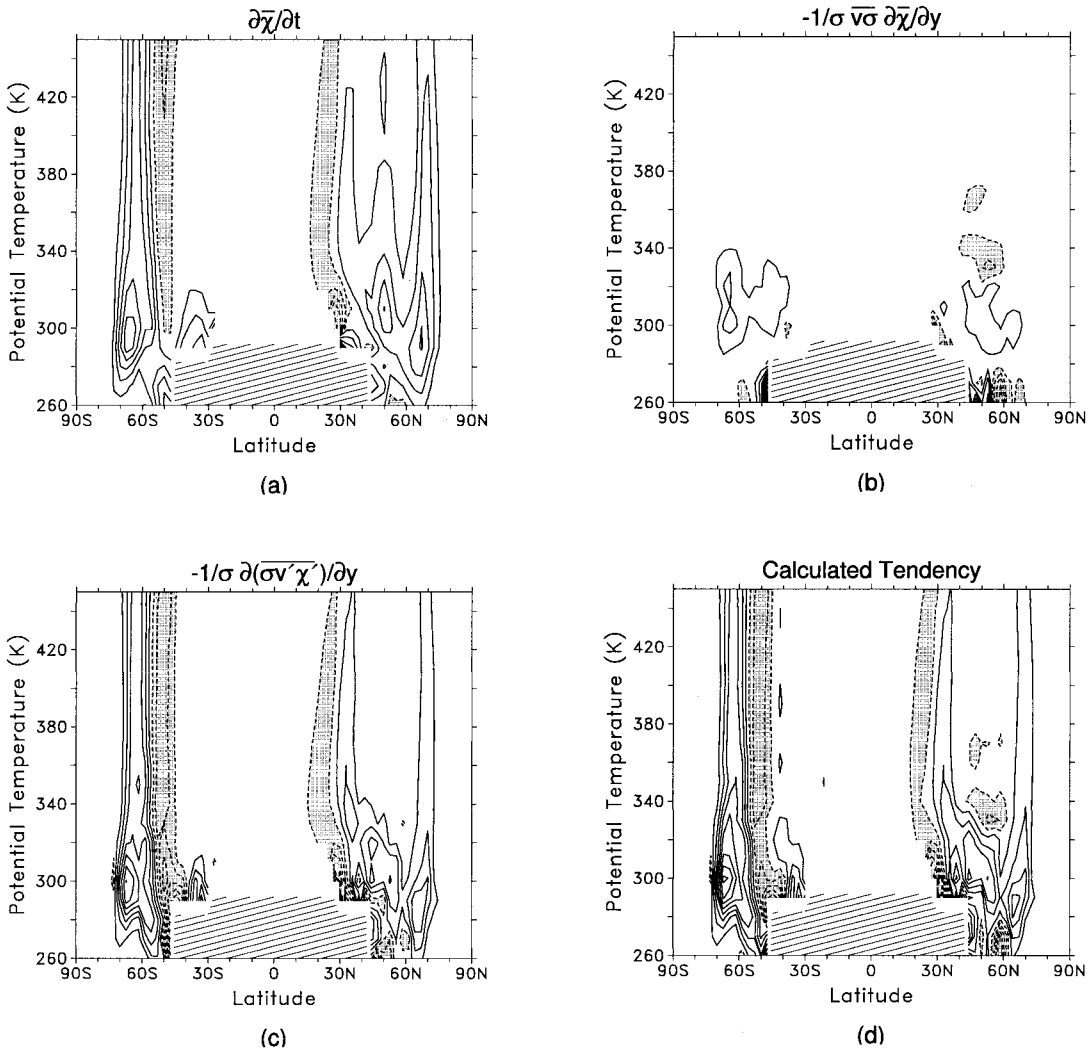

FIG. 13. Individual terms in the tracer continuity equation in isentropic coordinates [Eq. (3)] for the horizontally stratified tracer averaged over days 1–10 of the model simulation. Contours are of ± 0.3, 0.9, 1.5, . . . g kg^{-1} day^{-1}. Negative regions are shaded and hatch marks indicate regions without data.

of LCn and LCs. The horizontally stratified tracer on the 315-K surface is shown in Fig. 14 for days 6 and 8 of the life cycles. Overlaid are contours of the absolute value of potential vorticity, defined by

$$\mathrm{PV} = -g(\zeta + f)\partial\theta/\partial p, \qquad (4)$$

derived from the model winds and temperature fields. During the two days shown, the tracer and PV in LCn are drawn out equatorward from the middle latitudes and are advected anticyclonically. LCs shows cyclonic wrapping up of tracer and PV contours on day 8.

The PV and horizontally stratified tracer fields appear highly correlated in Fig. 14 and the description of the tracer matches the PV field on this surface (Figs. 4 and 5). In order to compare this more quantitatively, Fig. 15 displays a scatter diagram of the horizontally stratified tracer and the PV field at the start of the life cycle and during the peak transport period. These plots show the value of each field at every grid point (of both hemispheres) on the 315-K surface. The initial relationship shows a one-to-one correspondence between the constituent and PV. Although the two fields are still fairly well correlated on day 7, the exact initial relationship does not remain intact and the correspondence between the two fields is smeared out, particularly in the extratropical values. A similar result is found in comparing individual tracers (not shown).

Zapotocny et al. (1996) and Zapotocny et al. (1997) examined the ability of the CCM2 to transport and conserve distributions of PV and an inert tracer. Their findings suggest that the two do not remain highly correlated due to details of the numerical transport scheme, and that amplifying baroclinic waves, wherein three-dimensional transport in the presence of vertical wind shear

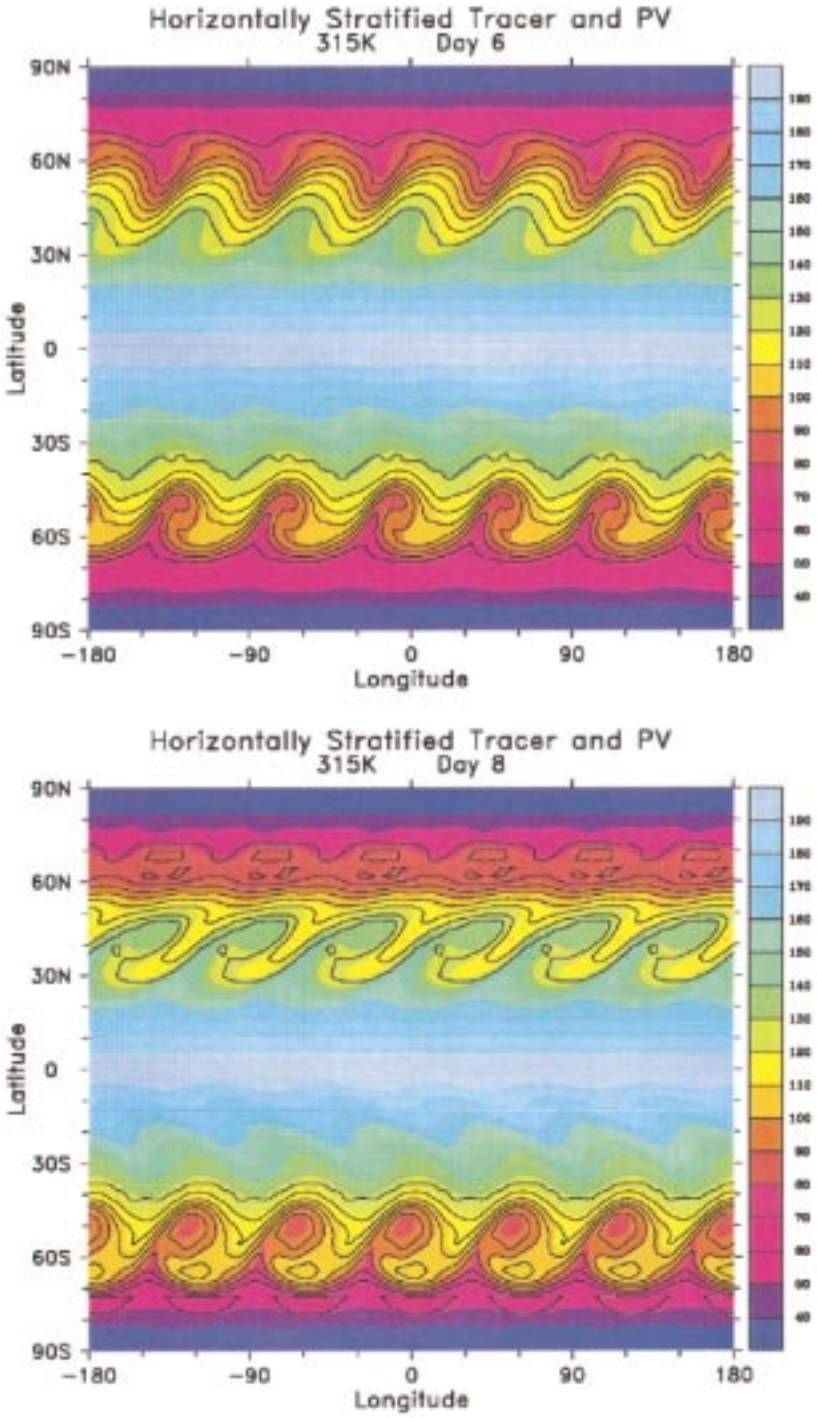

FIG. 14. Latitude–longitude plots of the horizontally stratified tracer and PV on the 315-K surface for days 6 and 8 of the model run. Color contours show the tracer field in kg kg^{-1}. Overlaid contours denote the absolute value of PV (0.5, 1, 2, . . . PVU; 1 PVU = 10^{-6} m^2 K s^{-1} kg^{-1}.)

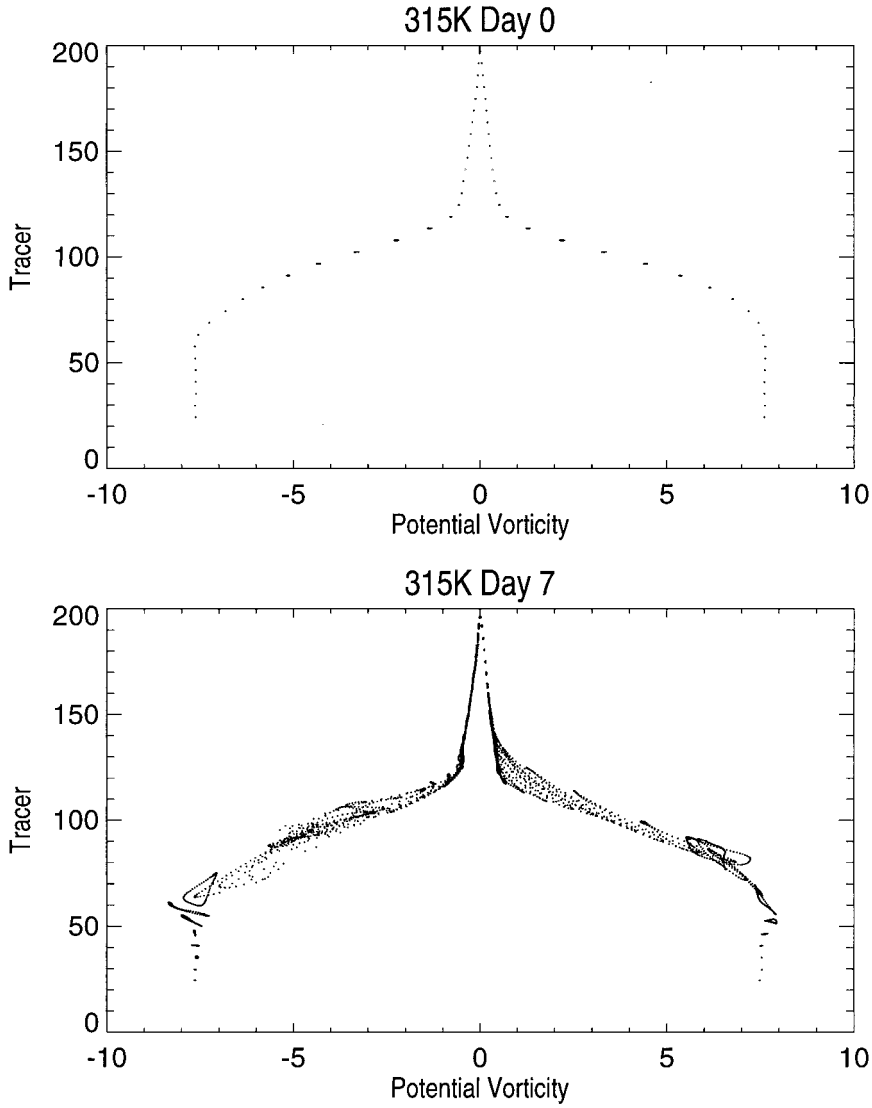

FIG. 15. Scatter diagram comparing the horizontally stratified tracer mixing ratio with the calculated PV field on the (top) initial day and (bottom) day 7 of the model run for all model grid points on the 315-K potential temperature surface.

must be resolved, leads to spurious decorrelation. This suggests that the reason the exact initial relationships between the tracers in Fig. 15 do not remain intact is due to the numerical transport scheme and is not caused by physical processes associated with the baroclinic waves, particularly since we are using an adiabatic version of the CCM2.

e. Stratospheric tracer

In the midlatitudes, isentropic surfaces traverse the troposphere and lowermost stratosphere, and isentropic mixing is an effective mechanism for stratosphere–troposphere exchange (see Holton et al. 1995). In this region, baroclinic waves are a predominant source of quasi-horizontal mixing on the isentropic surfaces (as shown in section 4c above). Recent studies have focused on the transport across the tropopause in the extratropics (Mote et al. 1994; Chen 1995; Rood et al. 1997). Mote et al. (1994) show that in the extratropics, exchange from the stratosphere to the troposphere occurs mainly in developing baroclinic waves and stationary anticyclones. In order to examine the issue of transport in the region of the tropopause during the two baroclinic wave life cycles of this study, a passive tracer is initialized with a value of 1 in the stratosphere (above the tropopause) and a value of 0 in the troposphere (this is a zeroth-order representation of ozone mixing ratio, for example). The tropopause is defined here by the 2-PVU level in the midlatitudes and the 380-K surface in the Tropics and is shown in the top panel of Fig. 16. A fundamental problem in quantifying transport across the

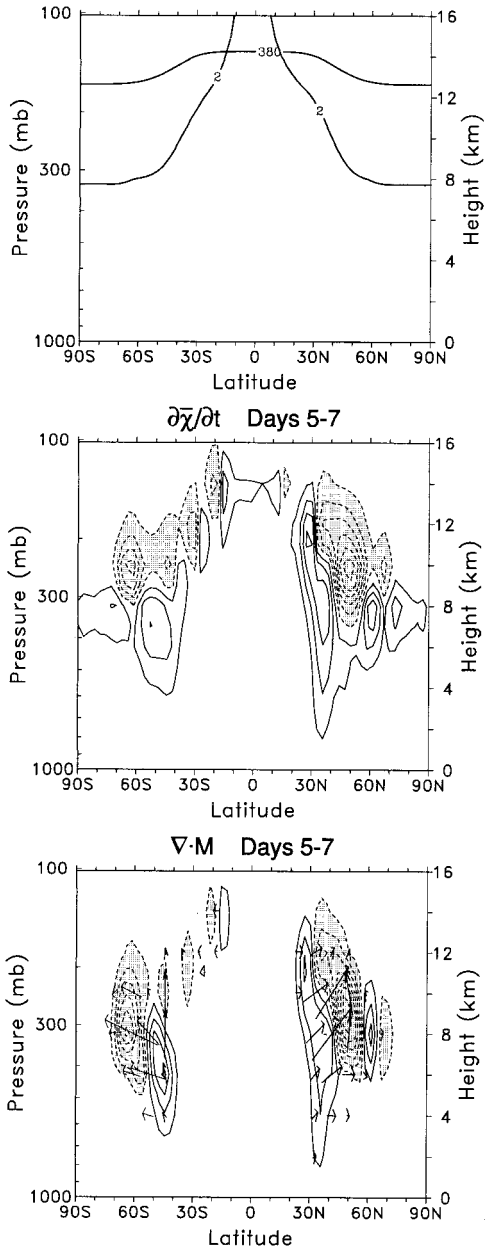

FIG. 16. Meridional cross sections of the tropopause (top) as defined by the 2 PVU and the 380-K potential temperature locations; the tendency of the stratospheric tracer (middle); and the eddy flux divergence of the stratospheric tracer along with vectors representing the eddy flux (bottom).

tropopause (defined by the PV = 2 PVU surface) in these life cycles is that both the tracer and PV fields are deformed in time in a nearly identical manner (see Fig. 14 and discussion above), so that both the tracer and 2 PVU contours change coherently. Hence, there is zero net tracer transport across the tropopause (apart from small numerical changes). This behavior also occurs in the real atmosphere to some degree, but radiative and other diabatic effects act to dissipate small-scale PV structures and restore the tropopause close to a climatological location. These diabatic effects do not act to restore the transported tracer, so there is a net transport across the tropopause (see Lamarque and Hess 1994; Wirth 1995). Because the baroclinic wave simulations here are adiabatic, the restoring effect on the tropopause is not simulated, and we cannot calculate the details of the processes described above. However, a qualitative estimate of the behavior of stratosphere–troposphere exchange can be made by calculating the tracer transport with respect to the initial (day 0) tropopause location. This assumes that the final tropopause position (after dissipation of the baroclinic waves and diabatic restoring effects) will be near the initial position shown in Fig. 16. Thus, we treat the zonal mean transport of the stratospheric tracer as an estimate of stratosphere–troposphere exchange. Although this is admittedly only a qualitative calculation, we feel it is a reasonable estimate given the limitations of an adiabatic simulation.

During the model run, the stratospheric tracer is transported with respect to the day-0 tropopause as the baroclinic waves develop. The middle panel of Fig. 16 shows the tendency of the stratospheric tracer averaged over days 5–7 of the model ran. The tendency field indicates that the tracer value has increased, from an original null value, just below the tropopause and decreased just above it. In the LCn case, the tendencies are somewhat larger and the stratospheric tracer is transported to lower altitudes (down to 2 km in Fig. 16) than that seen in the LCs case. Figure 16 also displays the eddy tracer flux divergence and vectors for the stratospheric tracer. Again, good agreement is seen between the tracer tendency and the eddy flux divergence terms of Eq. (1), demonstrating that eddy transport is the dominant mechanism of the exchange. The eddy tracer flux vectors point upward and poleward signifying an equatorward and downward flux of tracer. Note this transport has increased the tracer mixing ratio in the (day 0) troposphere and decreased it in the (day 0) lowermost stratosphere; that is, there is a two-way exchange across the initial tropopause location. We quantify this exchange and find that nearly 4% of the tracer mass initially present in the lowermost stratosphere is located at altitudes below the initial location of the tropopause by day 10.

5. Summary and discussion

In this study we utilize the NCAR CCM2 to study two baroclinic wave life cycles, LCn and LCs. The initial differences in the horizontal zonal wind shear of the two cases produced two different life cycle evolutions, described briefly in section 3. A more complete description of the two life cycle paradigms is given by THM. While the eddy kinetic energy evolution of the two life cycles is very similar, their distinct dynamical features are seen in the EP flux diagnostics and the cyclonic and anticyclonic behavior of their isentropic

potential vorticity fields. The results presented here are fairly consistent with those of THM for LC1 and LC2, with the difference being the faster decay of the LCs case compared with LC2.

The simulation of idealized baroclinic wave life cycles provides a tool for the study of constituent transport in the troposphere where baroclinic wave activity is a dominant feature. In this study we address the transport of four passive tracers, which occurs during LCn and LCs: we quantify how the two life cycles affect the details of transport characteristics, and how the results are influenced by the initial tracer distributions. The net transport characteristics are analyzed by their zonal mean and synoptic descriptions, and are quantified using the TEM and isentropic tracer equation formalisms.

Results show that the effect on the zonal mean mixing ratios is that of downgradient constituent transport during the life cycles, but with characteristic spatial patterns maximizing in the middle–high latitudes. For the horizontally stratified, the vertically stratified, and the midlatitude tracers of this study, this results in increasing tracer values in the middle and upper troposphere in the 55°–75° latitudinal range and decreasing values at the lower levels in the 30°–60° range.

The TEM tracer equation formalism shows that the tendency of the tracer field is influenced most strongly by the eddy transport term, with very little contribution from the transport by the mean residual circulation. There is a strong similarity between the TEM transport calculations in log pressure coordinates and isentropic coordinate results; the latter also demonstrate that isentropic mixing dominates transport in these life cycles. Calculations of the balance in the TEM log pressure and isentropic tracer conservation equations show good agreement between the calculated and measured tendencies. The characteristics of transport in the meridional plane, shown by the tracer tendency and the eddy tracer flux divergence and vectors, show similar characteristics for LCn and LCs. However, LCn exhibits a broader meridional structure of the tracer transport as compared to LCs with transport effects reaching the subtropics. The transport due to LCs is more confined to high latitudes. The broader meridional structure of the tracer transport in LCn is consistent with the larger meridional extent of the wave in LCn as compared to LCs, shown in Figs. 4, 5, and 14.

In addition to the similarities seen between the two life cycles, the structure of the time tendency of the tracer transport varies little with the initial constituent fields, even in the two orthogonally constructed tracers. This may be unexpected since the eddy tracer flux divergence and vectors [Eq. (2)] depend upon the horizontal and vertical gradients of the tracer fields. However, as the baroclinic wave develops, gradients in the tracer fields are created that eliminate the perfect horizontal or vertical stratification in the midlatitudes that is present initially, thus allowing for both eddy flux terms to be influential.

In order to isolate the transport across the tropopause during the two life cycles, we initialize a run with a constituent in the stratosphere only. On the timescale of the baroclinic wave event, transport of the constituent across the initial position of the tropopause is clearly seen, with rapid two-way exchange between the (day 0) stratosphere and troposphere. Nearly 4% of the tracer mass initialized in the lowermost stratosphere on day 0 is transported to regions below the initial location of the tropopause over the 10 days of the life cycle simulation.

Acknowledgments. The National Center for Atmospheric Research is sponsored by the National Science Foundation. We thank R. Saravanan and Dave Erickson for helpful comments on this work. We also thank an anonymous reviewer for suggesting inclusion of the isentropic transport calculations. EMS acknowledges the support from the Atmospheric Chemistry Division of NCAR and the Graduate Assistance in Areas of National Need fellowship from the U.S. Department of Education and Iowa State University. WJR is supported by NASA Grants W-18181 and W-16215. JLS is supported by NASA Grant 5-2787.

REFERENCES

Andrews, D. G., J. R. Holton, and C. B. Leovy, 1987: *Middle Atmosphere Dynamics.* Academic Press, 489 pp.

Barnes, J. R., and R. E. Young, 1992: Nonlinear baroclinic instability on a sphere: Multiple life cycles with surface drag and thermal damping. *J. Atmos. Sci.,* **49,** 861–878.

Branscome, L. E., W. J. Gutowski Jr., and D. A. Stewart, 1989: Effect of surface fluxes on the nonlinear development of baroclinic waves. *J. Atmos. Sci.,* **46,** 460–475.

Chen, P., 1995: Isentropic cross-tropopause mass exchange in the extratropics. *J. Geophys. Res.,* **100,** 16 661–16 674.

Edmon, H. J., B. J. Hoskins, and M. E. McIntyre, 1980: Eliassen–Palm cross sections for the troposphere. *J. Atmos. Sci.,* **37,** 2600–2616.

Erickson, D. J., and Coauthors, 1996: The seasonal cycle of atmospheric CO_2: A study based on the NCAR Community Climate Model (CCM2). *J. Geophys. Res.,* **101,** 15 079–15 087.

Gutowski, W. J., Jr., L. E. Branscome, and D. A. Stewart, 1989: Mean flow adjustment during life cycles of baroclinic waves. *J. Atmos. Sci.,* **46,** 1724–1737.

——, ——, and ——, 1992: Life cycles of moist baroclinic eddies. *J. Atmos. Sci.,* **49,** 306–319.

Hack, J. J., B. A. Boville, B. P. Briegleb, J. T. Kiehl, P. J. Rasch, and D. L. Williamson, 1993: Description of the NCAR Community Climate Model (CCM2). NCAR Tech. Note NCAR/TN-382+STR, 108 pp.

——, ——, J. T. Kiehl, P. J. Rasch, and D. L. Williamson, 1994: Climate statistics from the National Center for Atmospheric Research Community Climate Model CCM2. *J. Geophys. Res.,* **99,** 20 785–20 813.

Hamilton, K., 1983: Aspects of wave behavior in the mid- and upper troposphere of the Southern Hemisphere. *Atmos.–Ocean,* **21,** 40–54.

Hartley, D. E., D. L. Williamson, P. J. Rasch, and R. G. Prinn, 1994: Examination of tracer transport in the NCAR CCM2 by comparison of CFC13 simulations with ALE/GAGE observations. *J. Geophys. Res.,* **99,** 12 885–12 896.

Hartmann, D. L., 1995: A PV view of zonal flow vacillation. *J. Atmos. Sci.,* **52,** 2561–2576.

Holton, J. R., P. H. Haynes, M. E. McIntyre, A. R. Douglass, R. B. Rood, and L. Pfister, 1995: Stratosphere-troposphere exchange. *Rev. Geophys.,* **33** (4), 403–439.

Hoskins, B. J., M. E. McIntyre, and A. W. Robertson, 1985: On the use and significance of isentropic potential vorticity maps. *Quart. J. Roy. Meteor. Soc.,* **111,** 877–946.

Lamarque, J.-F., and P. G. Hess, 1994: Cross-tropopause mass exchange and potential vorticity budget in a simulated tropopause folding. *J. Atmos. Sci.,* **51,** 2246–2269.

Lee, S., and S. Feldstein, 1996: Two types of wave breaking in an aquaplanet GCM. *J. Atmos. Sci.,* **53,** 842–857.

Magnusdottir, G., and P. H. Haynes, 1996: Wave activity diagnostics applied to baroclinic wave life cycles. *J. Atmos. Sci.,* **53,** 2317–2353.

Mote, P. W., J. R. Holton, and J. M. Wallace, 1991: Variability in total ozone associated with baroclinic waves. *J. Atmos. Sci.,* **48,** 1900–1903.

——, ——, and B. A. Boville, 1994: Characteristics of stratosphere-troposphere exchange in a general circulation model. *J. Geophys. Res.,* **99,** 16 815–16 829.

Palmer, T. N., 1982: Properties of the Eliassen–Palm flux for planetary scale motions. *J. Atmos. Sci.,* **39,** 992–997.

Randel, W. J., and J. L. Stanford, 1985a: An observational study of medium-scale wave dynamics in the Southern Hemisphere summer. Part I: Wave structure and energetics. *J. Atmos. Sci.,* **42,** 1172–1188.

——, and ——, 1985b: The observed life cycle of a baroclinic instability. *J. Atmos. Sci.,* **42,** 1364–1373.

——, and I. M. Held, 1991: Phase speed spectra of transient eddy fluxes and critical layer absorption. *J. Atmos. Sci.,* **48,** 688–697.

Rasch, P. J., and D. L. Williamson, 1990: Computational aspects of moisture transport in global models of the atmosphere. *Quart. J. Roy. Meteor. Soc.,* **116,** 1071–1090.

Rood, R. B., A. R. Douglass, M. C. Cerniglia, and W. G. Read, 1997: Synoptic-scale mass exchange from the troposphere to the stratosphere. *J. Geophys. Res.,* **102,** 23 467–23 485.

Salby, M. L., 1982: A ubiquitous wavenumber-5 anomaly in the Southern Hemisphere during FGGE. *Mon. Wea. Rev.,* **110,** 1712–1720.

Schoeberl, M. R., and A. J. Krueger, 1983: Medium-scale disturbances in total ozone during Southern Hemisphere summer. *Bull. Amer. Meteor. Soc.,* **64,** 1358–1365.

Simmons, A. J., and B. J. Hoskins, 1978: The life cycles of some nonlinear baroclinic waves. *J. Atmos. Sci.,* **35,** 414–423.

——, and ——, 1980: Barotropic influences on the growth and decay of nonlinear baroclinic waves. *J. Atmos. Sci.,* **37,** 1679–1684.

Stone, E. M., W. J. Randel, J. L. Stanford, W. G. Read, and J. W. Waters, 1996: Baroclinic wave variations observed in MLS upper tropospheric water vapor. *Geophys. Res. Lett.,* **23,** 2967–2970.

Thorncroft, C. D., B. J. Hoskins, and M. E. McIntyre, 1993: Two paradigms of baroclinic-wave life-cycle behaviour. *Quart. J. Roy. Meteor. Soc.,* **119,** 17–55.

Williamson, D. L., and P. J. Rasch, 1989: Two-dimensional semi-Lagrangian transport with shape preserving interpolation. *Mon. Wea. Rev.,* **117,** 102–129.

——, and ——, 1994: Water vapor transport in the NCAR CCM2. *Tellus,* **46A,** 34–51.

Wirth, V., 1995: Diabatic heating in an axisymmetric cut-off cyclone and related stratosphere–troposphere exchange. *Quart. J. Roy. Meteor. Soc.,* **121,** 127–147.

Zapotocny, T. H., A. J. Lenzen, D. R. Johnson, F. M. Reames, P. A. Politowicz, and T. K. Schaack, 1996: Joint distributions of potential vorticity and inert tracer constituent in CCM2 and UW θ-σ model simulations. *Geophys. Res. Lett.,* **23,** 2525–2528.

——, ——, ——, T. K. Schaack, and F. M. Reames, 1997: A comparison of inert tracer constituent transport between the University of Wisconsin isentropic-sigma model and the NCAR Community Climate Model. *Mon. Wea. Rev.,* **125,** 120–142.